Models and modeling schemes for binary IV-VI glasses

De Nyago Tafen and D. A. Drabold

Department of Physics and Astronomy, Ohio University, Athens, Ohio 45701

In this paper, we present and thoroughly characterize several new models of amorphous binary IV-VI glasses. We apply both a quench from the melt simulation regime and a scheme based on decoration of tetrahedral amorphous networks. We show that for certain binary IV-VI glasses (especially silica), decoration of bond-centered column VI atoms on tetrahedral amorphous networks leads with appropriate re-scaling and relaxation to highly realistic models of the IV-VI glass. In particular, the problem of freezing in too much liquid-like character seems to be significantly ameliorated. We also carry out first-principles molecular dynamics simulations to study the structural, dynamical, and electronic properties of $GeSe_4$ and $GeSe_9$. Good agreement with experiment is obtained for the total neutron structure factor over the entire range of k-space and for the electronic density of states.

I. INTRODUCTION

The nature and extent of atomic ordering in amorphous solids has attracted considerable interest and has accelerated recently. This is partly because of an increase in the technological utility of glasses in various applications. It is also part of a general interest in the fundamental properties of disordered materials. For example, amorphous silicon dioxide constitutes a prototypical example of a network-forming disordered material[1] and is important for geophysics and for electronic applications. The Raman spectrum of g-$SiSe_2$ gives the clearest indication of the presence of intermediate-range structural order (IRO) of any chalcogenide.[2] There is also a pressing need for ways to build models of non-stoichiometric glasses.

To produce realistic models, Nakhmanson, Zhang, and Drabold[3] have found it useful to include primitive *a priori* information about the chemical order and coordination in model construction because of the limitations of molecular dynamics (MD) simulation time scales. For Ge_xSe_{1-x}, the limitation of the quench from the melt method appears to be an incorrect static structure factor $S(Q)$, for large Q. We have recently developed a new scheme, "decorate and relax,"[4] to produce binary glasses from models of tetrahedral amorphous semiconductors. We have made a comparison of such models to those obtained from quench from the melt process. Encouraging agreement with the existing experimental data was obtained especially for large Q behavior of $S(Q)$.[4] For large Q, $S(Q)$ for the quench from the melt models decays away too rapidly relative to experiments.[6] In parallel work we are developing a scheme "Experimentally constrained molecular relaxation" to enable direct inclusion of experimental data in model formation.[5]

In this paper we carry out model calculations on AX_2 (A≡Si, Ge and X≡Se, O) using decorate and relax. We also model Ge_xSe_{1-x} (x=0.1, 0.2) using the quench from the melt technique. To our knowledge there is little experimental and theoretical work on the structure and vibrational structure of g-$GeSe_4$, and nothing on electronic structure. Compositions near g-$GeSe_4$ are used as a host for Ag^+ ions and

the Programmable Metallization Cell.[7] In a joint experimental and theoretical study of g-$GeSe_9$, Rao *et al.*[8] limited their work only to the static structure factor and the pair distribution function. They have suggested that g-$GeSe_9$ consists predominantly of Se-chain segments interlinked with tetrahedra. Theirs is the first attempt to carry out theoretical work on the vibrational and electronic structure of g-$GeSe_9$ glass. We demonstrate the utility of our simulations by performing detailed comparison with experimental data (where available) in real and k-space and by comparing to vibrational and electronic measurements where available.

The rest of the paper is organized as follows. In the next section we give a brief description of our simulation methods and model generation. Section III describes the structural properties of our different models by looking at the structure factors, pair correlation functions, and ring distribution. Section IV is devoted to the vibrational properties of the models. The electronic properties of the systems are examined in section V, and Sec. VI provides discussion of the composition dependence of experimental observables for GeSe binary glasses.

II. MODEL GENERATION

A. Total energy/force codes

For some of the simulations reported in this paper, we used FIREBALL, an approximate *ab initio* density functional code in the LDA developed by Sankey and co-workers.[9] In this method the Harris functional is used in a scheme with the mathematical structure of nonorthogonal tight-binding,[10] and the use of no free parameters in constructing the Hamiltonian matrix. The basis set is minimal (for these systems, one s and three p slightly excited pseudo-atomic orbitals per site). This scheme does well at producing experimentally credible models because of its balance between accuracy and efficiency. In particular, experimentally realistic models require large supercell models and long time evolutions in addition to a suitable level of accuracy, which FIREBALL provides. The other code is SIESTA,[11] which has broad flexibility with respect to basis set, density functional, and simulation
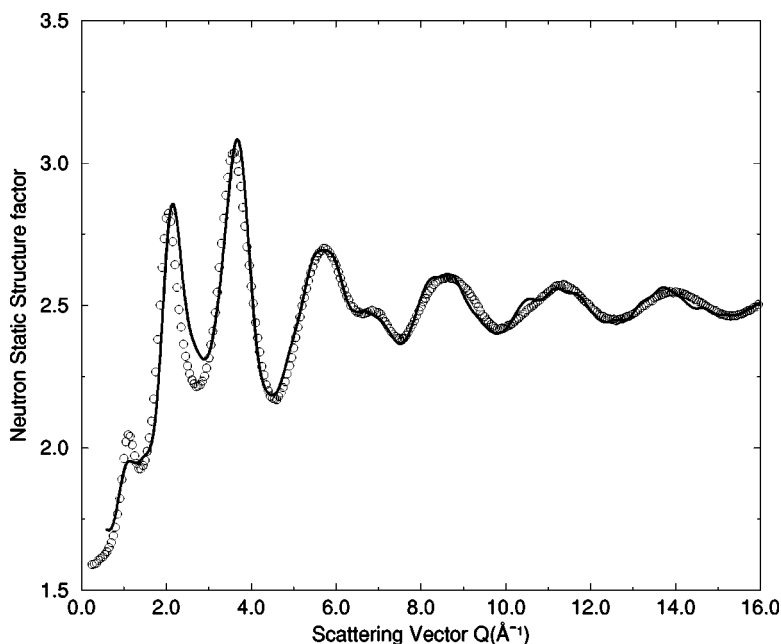
FIG. 1. Calculated total neutron structure factor $S(Q)$ of quench from the melt glassy $GeSe_4$ (solid line) compared to experimental (Ref. 14) data (circle). We used scattering lengths of b_{Ge} $=8.185$ and $b_{Se}=7.970$ fm.

regime. We employed SIESTA for silica because the extreme ionicity of the material, and also to easily check the importance of density functional, basis set and spin polarization.

B. Model formation

The models described here have been generated using the decorate and relax method, except g-$GeSe_4$ and g-$GeSe_9$. The details of the method were reported in Ref. 4 and Ref. 5. We just give a brief recap here. The starting point is a defect-free (fourfold coordinated) atom supercell model of a-Si made with the WWW method[12] as further developed by Barkema and Mousseau.[13] We decorated all the IV-IV bonds with a bond-center VI, and rescaled the coordinates to the experimental density of the model. In this way we made 648-atom models of g-$GeSe_2$, g-$SiSe_2$, and g-SiO_2. The 648-atom models of g-$GeSe_2$ and g-$SiSe_2$ were then quenched with FIREBALL to the nearest minimum. The 648-atom model of g-SiO_2 was relaxed with SIESTA.

A 600-atom model of g-$GeSe_4$ was made using the quench from the melt technique. We randomly placed atoms in a cubic supercell with edge length 26.061 Å. The initial temperature of our system was 2400 K. We then equilibrated the cell at 1400 K for approximately 4 ps. After equilibration, we began quenching it down to about 700 K over 4 ps. As the final step, we steepest descent quenched the cell to 0 K and forces smaller in magnitude than 0.02 eV/Å.

To model g-$GeSe_9$ we randomly placed atoms in a cubic supercell, (consisting of 40 Ge atoms and 360 Se atoms), with side length of 22.971 Å. This gives a total number density close to experiment (0.0330 Å^{-3}).[8] Then we brought the temperature of the system to 2200 K. We took three steps to cool down the model. First, the cell was equilibrated at 1400 K for over 2 ps; then we cooled it at 300 K for over 3 ps. Finally the cell was steepest descent quenched to 0 K.

All the calculations were performed at constant volume using the Γ point to sample the Brillouin zone in order to

compute energies and forces. Considering the large supercell volume it was reasonable to use Γ point alone. The final model of g-$GeSe_2$ consists of 216 Ge atoms and 432 Se atoms with lattice constant 27.525 Å, the g-SiO_2 consists of 216 Si atoms and 432 O atoms with the side length 21.39 Å, and g-$SiSe_2$ has 216 Si atoms and 432 Se atoms with lattice constant 27.6 Å.

III. STRUCTURAL PROPERTIES

Structural information can be extracted from the neutron static structure factor $S(Q)$. $S(Q)$ has been obtained by weighting the calculated partial structure factors with the neutron scattering lengths of the corresponding elements. The topology of the glasses can be described by the pair correlation function $G(r)$, which is related to $S(Q)$ by

$$G(r) = 1 + \frac{1}{4\pi\rho} \int_0^\infty [S(Q) - 1] \frac{Q^2 \sin(Qr)}{Qr} dQ.$$

The topology of our models is also analyzed with ring statistics. The ring structures in our models are determined by starting on a particular atom, moving to one of its neighbors, and then repeating this process for the neighbor until the original atom is located again after the desired number of iterations (making sure not to include any atom which is already part of the ring from a previous iteration since an n-fold ring consists of $2n$ alternating IV-VI bonds).

A. GeSe$_4$ glass

In Fig. 1 we compare the neutron static structure factor $S(Q)$ to the experiment of Petri and Salmon.[14] The first sharp diffraction peak (FSDP) is present in the quench from the melt model at 1.12 Å^{-1}; but it was absent in the decorated model.[4] We believe that the absence of the FSDP in the decorated model is a size effect since the decorated model con-

TABLE I. Average number $m_\alpha(l)$ (boldface characters, expressed as a percentage) of atoms of species α (α=Ge, Se) l-fold coordinated at a distance of 2.8 Å for GeSe$_4$. We also give the identity and the number of the Ge and Se neighbors for each value of $m_\alpha(l)$.

Ge		$l=2$	**2.5**	$l=3$	**8.33**
		Se$_2$	2.5	Se$_3$	8.33
$l=4$	**88.34**	$l=5$	**0.83**		
GeSe$_3$	11.67	Se$_5$	0.83		
Se$_4$	76.67				
Se		$l=1$	**17.30**	$l=2$	**63.54**
		Se	3.75	Se$_2$	19.79
		Ge	13.55	SeGe	25
				Ge$_2$	18.75
$l=3$	**19.16**				
Se$_3$	8.54				
Se$_2$Ge	3.54				
SeGe$_2$	2.5				
Ge$_3$	4.58				

FIG. 2. Partial pair distribution functions $g_{\alpha\beta}(r)$ vs r in g-GeSe$_4$ (dotted lines) and in g-GeSe$_9$ (solid lines).

sists of 319 atoms (a similar effect has been observed in our 190-atom model of g-GeSe$_4$ using quench from the melt) whereas the quench from the melt model has 600 atoms. The second peak depends on the next nearest neighbors at approximately 3.8 Å. From the partial structure factors, it is evident that the second peak is due to Se—Se correlations. There is still a slight discrepancy between the experimentally observed strength of the second peak and that of our $S(Q)$. Overall our calculated neutron structure factor is in agreement with the experimental results.

In our model the very prominent FSDP is clearly seen in $S_{CC}(Q)$ at around 1.08 Å^{-1} which implies that the strong Ge—Ge IRO correlations in g-GeSe$_4$ are reasonably well described. This feature does not, however, appear in classical MD simulations[15] of amorphous GeSe$_2$ and it has proved possible to reproduce this feature using the first principles MD approach of Massobrio *et al.*[16] only when a general gradient approximation is used in the density functional.

Where coordination is concerned, we note that 88.5% of Ge are fourfold coordinated and are mostly in GeSe$_4$ tetrahedral units, 8% are threefold coordinated and 3.5% are twofold and fivefold coordinated. Se is quite a different story: about 64% of the Se are twofold coordinated, 19% are threefold and about 17% are onefold coordinated. Where chemical order is concerned, g-GeSe$_4$ has 64.23% Ge—Se bonds, 0.9% Ge—Ge bonds, and 34.87% Se—Se bonds. In Table I we give a full description of the topology of our model. In Fig. 2 we plot the partial pair distribution function of g-GeSe$_4$. The peaks in $g_{\alpha\beta}(r)$ for distances larger than the nearest neighbor distance are a manifestation of the IRO in the system and $g_{\text{Ge—Ge}}(r)$ shows correlations between tetrahedra. There are two distinct peaks which correspond, respectively, to Ge—Ge first and second neighbors at 2.36 and 3.8 Å in $g_{\text{Ge—Ge}}(r)$. The broad peak between 3.0 and 4.3 Å in the $g_{\text{Ge—Ge}}(r)$ is caused by the presence of both corner
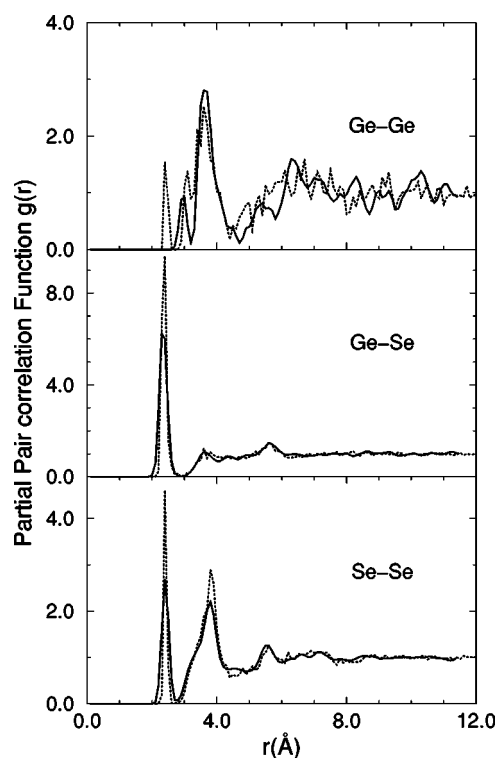
sharing (CS) (the tetrahedra shares one Se atom) and edge sharing (ES) tetrahedra (the tetrahedra shares two Se atoms). In $g_{\text{Ge—Ge}}(r)$ the first peak is located at 2.36 Å, which is quite close to the crystal Ge—Se bond length of 2.355 Å (for α-GeSe$_2$). The next peak appears at 3.7 Å and it is associated with CS units. Another peak arises at 5.65 Å which indicates that there is some kind of IRO in our model; the strength and width of this peak are due to Ge correlations with Se on neighboring tetrahedra. The $g_{\text{Se—Se}}(r)$ nearest-neighbor peak is located at approximately 2.32 Å. The second peak at approximately 3.78 Å is close to the Se—Se separation distance in crystalline α-GeSe$_2$.[17] Since the ratio of Ge—Se : Se—Se distances is 0.624, close to the value of 0.612 expected for perfect tetrahedral coordination, the results indicate that there is a large number of tetrahedral Ge(Se$_{1/2}$)$_4$ structural motifs and those tetrahedral units are distorted.

We also obtain partial n_{Ge}, n_{Se}, and average n coordination numbers from the first neighbor coordination numbers n_{GeGe}, n_{GeSe}, n_{SeGe}, and n_{SeSe} (see Table II) by integrating the partial pair correlation function $g_{\alpha\beta}(r)$. The theoretical Ge—Ge coordination number n_{GeGe} shows that each Ge atom has on average $n_{\text{GeGe}}=0.12$ nearest neighbors of the same species within a given shell of radius 2.8 Å. The predominant Ge—Se heteropolar bonding is expressed by a coordination number $n_{\text{GeSe}}=3.80$. The total Ge and Se coordination numbers, $n_{\text{Ge}}=n_{\text{GeGe}}+n_{\text{GeSe}}$, $n_{\text{Se}}=n_{\text{SeSe}}+n_{\text{SeGe}}$, are therefore 3.92 and 2.03, respectively. The average coordination number, $n=c_{\text{Ge}}n_{\text{Ge}}+c_{\text{Se}}n_{\text{Se}}$, gives a value $n=2.41$. The resulting values are very close to a perfect chemically ordered tetrahedral network (CON).

TABLE II. First and second peak positions in g-GeSe$_4$. Also first and second neighbor coordination numbers $n_{\alpha\beta}$ and $n'_{\alpha\beta}$. The integration ranges are 0–2.8, 2.8–4.5 Å for Ge—Ge and Se—Se; 0–3.0, 3.0–4.5 Å for Ge—Se and Se—Ge.

Bond type	First shell		Second shell	
	r(Å)	$n_{\alpha\beta}$	r'(Å)	$n'_{\alpha\beta}$
Ge—Ge	2.36	0.12	3.8	2.26
Ge—Se	2.36	3.80	3.7	—
Se—Ge	2.36	0.91	3.7	—
Se—Se	2.32	1.12	3.78	9.74

The topology of covalent glasses is commonly discussed in terms of rings. We have calculated the distribution of threefold to ninefold rings. The distributions of rings for the model are given in Table V. There is a predominance of fivefold and sixfold rings in the glass.

B. GeSe$_9$ glass

In Fig. 3 we compare the calculated neutron static structure factor $S(Q)$ for g-GeSe$_9$ to the experimental results from neutron diffraction measurements.[8] The general trend complies with observation though the detailed structure departs from the experimental data. The FSDP appears only as a shoulder; and it is more pronounced in our calculation than in experiment (though it is quite weak in both). Experimental studies[8,14] on Ge$_x$Se$_{1-x}$ have shown that the intensity of FSDP first increases systematically with Ge concentration, then reaches its maximum at $x=0.33$, then subsequently decreases. The third peak and the features at higher Q depend mainly on the local environment. As soon as the nearest neighbor atoms are taken into account, the third peak appears. On the other hand, the second peak in $S(Q)$ depends

on the next-nearest neighbors at approximately 4.3 Å. The shoulder in $S(Q)$ at around 1.04 Å^{-1} is due to the cancellation between $S_{GeGe}(Q)$ and $S_{SeSe}(Q)$.

Partial pair correlation functions $g_{\alpha\beta}(r)$ are shown in Fig. 2. The Ge—Se pairs provide the dominant contribution to the first shell of the pair correlation function. It is obvious that there exist Se—Se homopolar bonds in the model due to the surplus of Se atoms relative to the stoichiometric composition GeSe$_2$. Se—Se pairs make a strong contribution in the range of the second shell, whereas Ge—Ge pairs contribute most in the range of the third shell. In $g_{Ge—Ge}(r)$ there are two distinct peaks which correspond, respectively, to Ge—Ge second and third neighbors at 3.02 and 3.76 Å. In a-Ge the nearest neighbor Ge—Ge separation is known to be 2.463 Å.[18] The absence of a peak in the first shell of $g_{Ge—Ge}(r)$ is due to the absence of Ge—Ge homopolar bonds in our model. In $g_{Se—Se}(r)$ the first peak is located at 2.36 Å, and the next peak appears around 3.64 Å. The peak around 5.6 Å indicates that our model exhibits IRO.

About 92.5% of Ge atoms are fourfold coordinated, 5% are fivefold coordinated and 2.5% are threefold coordinated. Also, only 60% of Se atoms are twofold coordinated, 20.4% are threefold and about 19.6% are onefold coordinated. Where chemical ordered is concerned, g-GeSe$_9$ has 36.3% Ge—Se bonds and 63.7% of Se—Se bonds. The Ge—Ge homopolar bonds are nonexistent in our model. The detailed topology of our model is given in Table III. Our result is in accordance with the chemically ordered continuous random network[19] which predicts that for $x<0.33$, Se—Se bonds are present in addition to Ge—Se bonds. Similarly Ge rich glasses, i.e., $x>0.33$, contain Ge—Ge as well as Ge—Se bonds. The theoretical Ge—Ge coordination number, $n_{GeGe}=0.0$, confirms that each Ge atom does not have any nearest neighbors of the same species within a first shell of radius 2.8 Å. We also obtain partial n_{Ge}, n_{Se}, and average n coordination numbers (see Table IV for details). The Ge and Se coordination numbers are, respectively, 3.99 and 2; that gives
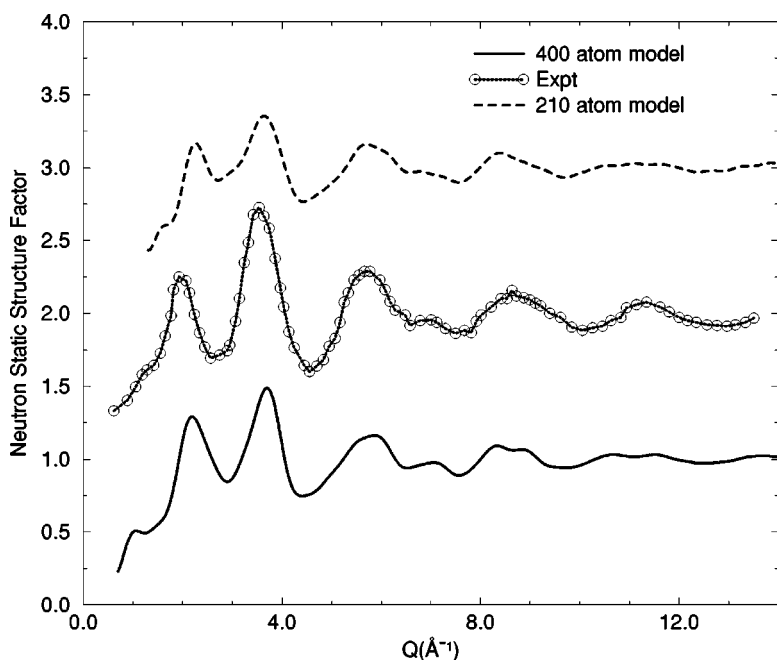

FIG. 3. Calculated total neutron structure factor $S(Q)$ of GeSe$_9$ (solid line) compared to experimental (Ref. 8) data (circle). We used scattering lengths of $b_{Ge}=8.185$ and $b_{Se}=7.970$ fm.

TABLE III. Average number $m_\alpha(l)$ (boldface characters, expressed as a percentage) of atoms of species α (α=Ge, Se), l-fold coordinated at a distance of 2.8 Å for GeSe$_9$. We also give the identity and the number of the Ge and Se neighbors for each value of $m_\alpha(l)$.

Ge		$l=3$	**2.5**	$l=4$	**92.5**
		Se$_3$	2.5	Se$_4$	92.5
$l=5$	**5**				
Se$_5$	5				
Se		$l=1$	**19.6**	$l=2$	**60**
		Se	7.1	Se$_2$	36.94
		Ge	12.5	SeGe	16.94
				Ge$_2$	6.12
$l=3$	**20.4**				
Se$_3$	16.78				
Se$_2$Ge	3.06				
SeGe$_2$	0.28				
Ge$_3$	0.28				

an average coordination number equal to 2.2. This number is quite reasonable since it lies between 2.16 for $x=0.08$ and 2.24 for $x=0.12$. Rao *et al.*[8] found a value of 2.45 for $x=0.1$.

There is a significant fraction of Ge(Se$_{1/2}$)$_4$ tetrahedral units in our model. The structure of the glass consists of Se-chain segments which are cross-linked by Ge(Se$_{1/2}$)$_4$ tetrahedra, as confirmed by n_{SeSe} and by visual inspection using XMOL.[20] We also note the presence of a few CS and a negligible fraction of ES. The structure of our model is also dominated by the presence of five- and six-member rings (see Table V).

C. SiO$_2$ glass

In Fig. 4 we compare the structure factor $S(Q)$ of our 648-atom model of g-SiO$_2$ with the $S(Q)$ of our 192-atom model[4] and the $S(Q)$ extracted from neutron diffraction experiments.[21] There is nearly perfect agreement with experiment over the entire range of Q. The height and the position of the peaks coincide with the experimental results.

TABLE IV. First and second peak positions in g-GeSe$_9$. Also first and second neighbor coordination numbers $n_{\alpha\beta}$ and $n'_{\alpha\beta}$. The integration ranges are 0–2.8, 2.8–3.23 Å for Ge—Ge; 0–2.8, 2.8–4.1 Å for Ge—Se and Se—Ge; 0–2.8, 2.8–4.34 Å for Se—Se.

	First shell		Second shell	
Bond type	r(Å)	$n_{\alpha\beta}$	r'(Å)	$n'_{\alpha\beta}$
Ge—Ge	—	0.0	3.02	0.11
Ge—Se	2.37	3.99	3.64	3.66
Se—Ge	2.37	0.44	3.64	0.58
Se—Se	2.35	1.56	3.79	9.2

TABLE V. Ring statistics. The number of n-membered rings, $n=3$ through $n=9$.

Ring size	3	4	5	6	7	8	9
GeSe$_4$	5	20	39	30	9	13	8
GeSe$_9$	2	3	15	6	2	4	2
SiO$_2$	0	7	0	6	0	15	0
SiSe$_2$	15	14	4	11	5	12	9

The discrepancy between the 192- and the 648-atom models arises from finite size effects, since the same Hamiltonian and modeling procedure was used to generate both models. It is of some interest that the only substantial difference between the 192- and 648-atom models was near 2.0 Å^{-1}, at the minimum after the FSDP. The only notable remaining discrepancy between theory and experiment appears near 12 Å^{-1}, and is similar to both models (and so is not due to a finite-size effect).

The origin of various peaks in $S(Q)$ can be inferred from partial structure factors. The results for partial static structure factors are shown in Fig. 5. The second peak in $S(Q)$ arises from Si—Si and O—O correlations with partial cancellation arising from Si—O anticorrelations. Since $S(Q)$ is weighted by concentrations and scattering lengths, the O—O contributions in this region are comparable to those of Si—Si. The third and fourth peaks receive contributions from Si—Si, O—O and Si—O correlations. The real space pair correlation functions of our vitreous silica models are illustrated in Fig. 6. The agreement between the experiment and theory is quite good. The peaks position and the bond lengths are well reproduced and comparable to experimental values from neutron diffraction data. On average, miscoordinated atoms in our 648-atom model occurred with a probability of 2.16%. These consisted of fivefold coordinated Si (3.2% of Si) and of threefold coordinated O (1.6% of O). Where chemical order is concerned, our model has 100% heteropolar bonding as one would expect from the chemistry of silica. The resulting amorphous model is characterized by the presence of chemically ordered bond network in which Si-atom-centered tetrahedra are linked by CS O atoms.

For vitreous silica we also compute the bond angle distribution. Figure 7 shows the distribution function for the tetrahedral angle O—Si—O and Si—O—Si. The O—Si—O angle has a mean value of 109.5° which is near the tetrahedral angle $\Theta_T=109.47°$, and a full width at half maximum (FWHM) of the order of 9°. On the other hand the Si—O—Si angle-distribution is much broader with an average value of 140° with a FWHM close to 25°. In their experiment,[22] Pettifer *et al.* obtained an average value of 142° for the angle Si—O—Si with a FWHM of the order of 26°. In Table VI we compare our results for the bond angle distribution with experiments[23,24] and theoretical results.[25] The location and the width of the peaks are in good agreement with experimental values. The topology of our model is also examined through the ring structure. In Table V we report the distributions of the rings in our sample. We notice that there is no contribution from odd rings. This reiterates
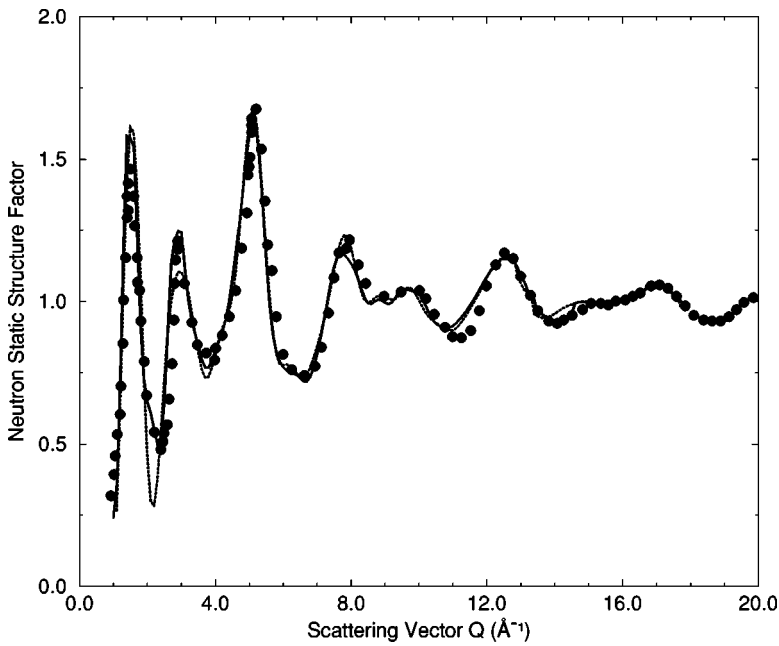
FIG. 4. Calculated total neutron static structure factor $S(Q)$ of glassy SiO_2 (dashed lines are for 192-atom model and solid lines are for 648-atom model) compared to experimental data (Ref. 21) (filled circles). We used scattering lengths of $b_{Si}=4.149$ and $b_O=5.803$ fm.

the absence of wrong bonds. We emphasize that the simple Decorate and Relax procedure seems extremely well suited to silica.

D. SiSe$_2$ glass

In Fig. 8 we display the calculated total neutron structure factor of our 648-atom model of g-SiSe$_2$ along with the

experimental[26] total neutron structure factor and the 192-atom model from decorate and relax.[4] The agreement is good over the entire q range, the positions of maxima and minima being properly reproduced (though the amplitudes are not perfect). Our calculated partial structure factors show a FSDP at 1.0 Å^{-1} in $S_{Si—Si}(Q)$ and $S_{Si—Se}(Q)$, and at 1.1 Å^{-1} in $S_{Se—Se}(Q)$. The largest value of the first sharp diffraction peak is observed in $S_{Si—Si}(Q)$ which is primarily responsible
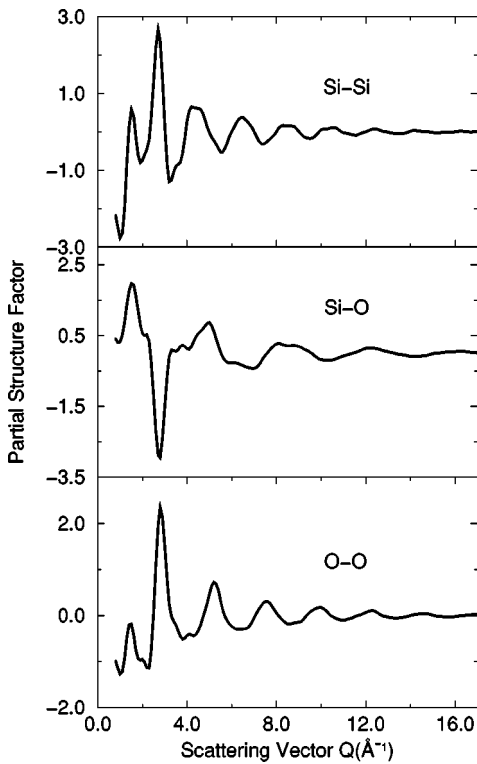

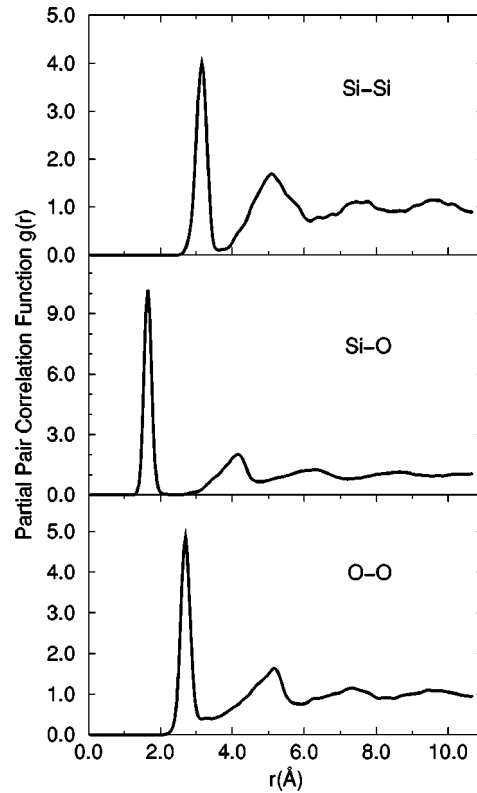FIG. 5. Calculated partial structure factors $S_{\alpha_\beta}(Q)$ of glassy SiO_2.

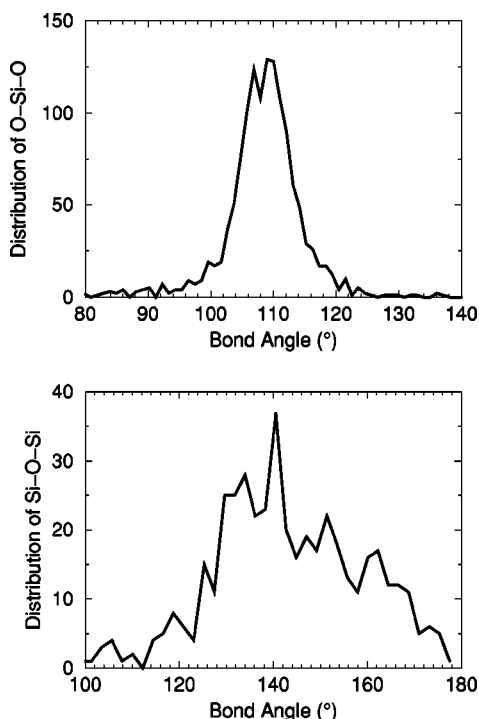FIG. 6. Calculated real space partial pair correlation function $g_{\alpha_\beta}(r)$ of g-SiO$_2$.

FIG. 7. Bond-angle distribution function O—Si—O (top panel) and Si—O—Si (bottom panel).

TABLE VI. Location, and in parentheses the FWHM of the angles O—Si—O and Si—O—Si as determined from the simulation and experiments.

	Theory		Experiment	
	Decorate	Ref. 25	Ref. 23	Ref. 24
OSiO	109.5° (9°)	108.3° (12.8°)	109.5°	109.7°
SiOSi	140° (25°)	152° (35.7°)	144° (38°)	144°, 152°

sists of both corner-sharing and edge-sharing $SiSe_4$ tetrahedra. The percentage of Si atoms forming homopolar bonds are less than 0.1%. On the other hand 6% of Se atoms are involved in homopolar bonding. Considering only the chemically ordered $SiSe_4$ and $SiSe_2$, about 80% of Si and 83.3% of Se atoms are, respectively, fourfold and twofold. Neutron diffraction and EXAFS experiments have suggested that the network of tetrahedra is mostly chemically ordered, but a small amount of homopolar bonds should not be ruled out.[28]

Few MD studies have determined ring statistics in amorphous $SiSe_2$.[29,30] Analysis of ring distributions (see Table V) reveals that threefold, fourfold, and eightfold are most abundant. In their calculations, Antonio et al.[30] found that threefold and eightfold rings were the most abundant, and chainlike fragments were revealed predominantly in eightfold rings. The appearance of odd number rings is due to homopolar bonds. There is also a significant amount of sixfold rings which together with the fourfold units are responsible for the chemical order in the glass.

for its appearance in the total neutron structure factor. In Celino and Massobrio's calculations[27] the FSDP was absent in the calculated Se—Se partial structure factor. To our knowledge, no experimental partial structure factors are currently available.

The MD partial pair correlation functions $g_{\alpha\beta}(r)$ for the 648-atom model are not so different from the 192-atom model[4] except for the appearance of a peak at around 3 Å in $g_{Si—Si}(r)$. This peak is entirely due to correlations arising from ES tetrahedra. The atomic structure of our model con-

IV. DYNAMICAL PROPERTIES

The vibrational properties are characterized by the vibrational density of states (VDOS) and species-projected vibrational density of states. Since the VDOS can be determined
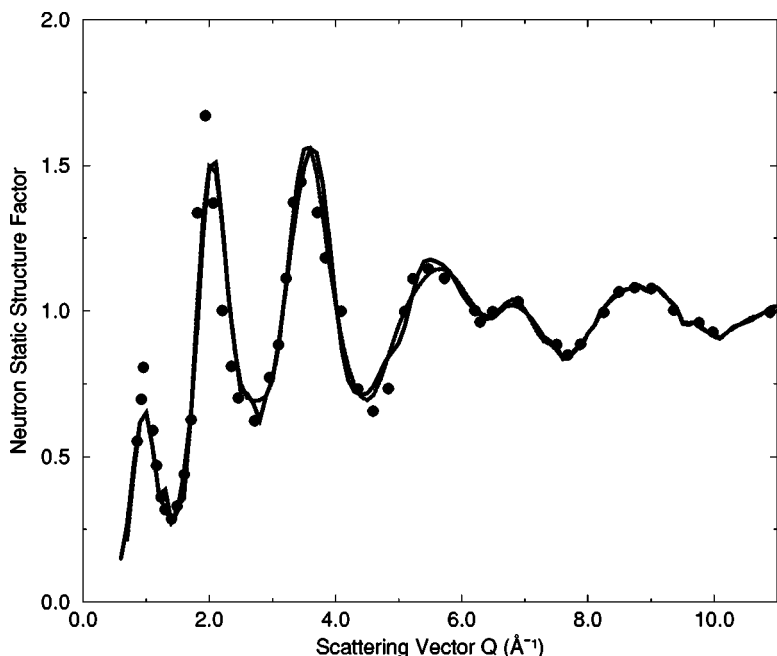

FIG. 8. Calculated total neutron static structure factor $S(Q)$ of glassy $SiSe_2$ (dotted lines are for 192-atom model and solid lines are for 648-atom model) compared to experimental data (Ref. 26) (filled circles). We used scattering lengths of $b_{Si}=4.149$ and $b_{Se}=7.970$ fm.
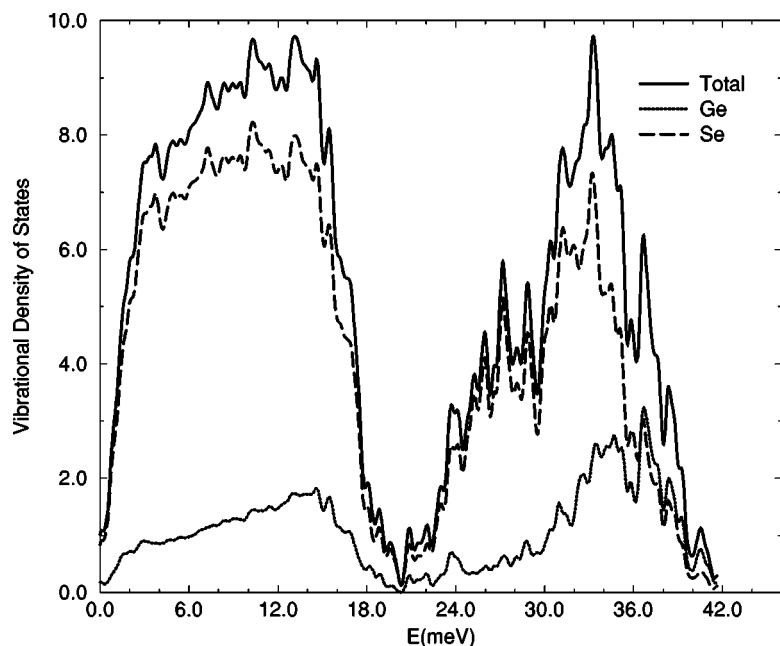
FIG. 9. Vibrational density of states (solid lines) and species projected vibrational density of states for Se (dashed lines) and Ge (dotted lines) for g-GeSe$_4$.

through inelastic neutron scattering, it provides a straightforward test of our models. The method has been described in previous work.[31] As a brief reminder, the supercell normal mode eigenvalues and eigenvectors were obtained from the dynamical matrix which was determined by displacing each atom by 0.015 Å in three orthogonal directions and then performing *ab initio* force calculations for all the atoms for each such displacement to obtain a column of the force constant matrix.

A. GeSe$_4$ glass

The vibrational density of states are plotted in Fig. 9. We also plot the species-projected density of states for Se and Ge. Three bands can be distinguished: a low energy acoustic band which is strongly correlated to the connectivity of the network involving mainly extended inter-block vibrations and a high energy optic band which tends to strongly depend on the configurations of the building blocks, consisting of more localized intrablock vibrations. The two main bands are clearly separated by the tetrahedral breathing (A_1-A_{1c}) band. The same features have been observed experimentally by Effey and Cappelletti,[32] also by Kamitakahara *et al.*[33] Effey and Cappelletti concluded that the broad band below 20 meV (161.31 cm^{-1}) is dominated by modes extending widely over the entire network and not by modes localized on "molecular" features in the glass such as the tetrahedron giving rise to the A_1 mode. Low frequency and high frequency characteristics are well reproduced. The species projected VDOS for the Se atoms and Ge atoms clearly show that the Se atoms are responsible for most of the motion.

B. GeSe$_9$ glass

In Fig. 10 we display the calculated VDOS and the species projected density of states of g-GeSe$_9$. The VDOS can be divided mainly into two bands. The low-energy band goes

up to 19 meV, and the high-energy band that decays near 40 meV. The shoulder around 19 meV and the sharp peak around 31 meV can be regarded, respectively, as the bond-bending and the bond-stretching vibrations. In the valley between the low-energy and the high-energy band, a feature arises at about 23.4 meV. This feature has been identified in Raman scattering measurements[34,35] as an A_1 mode resulting from vibrations of Se atoms with their cross-linking Ge neighbors. This feature is absent in the spectrum of Se. Experimentally,[33] it has been shown that the A_1 mode is a function of Ge concentration in the glass. As Ge concentration increases, the A_1 mode rises in the gap.

C. SiO$_2$ glass

Amorphous silica has been extensively characterized via vibrational spectroscopies, including inelastic neutron scattering,[36] infrared absorption,[37] and Raman scattering experiments.[38] It was found that the spectrum shows several peaks. In order to show the validity of the vibrational features of our model, we report in Fig. 11 the VDOS for the 192-atom model of g-SiO$_2$ (the dynamical matrix for the 648 atom model has not yet been calculated) along with the neutron scattering experimental results of Carpenter *et al.*[36] Shapes and positions of the principal peaks are well reproduced with low-frequency bands at 400 and 495 cm^{-1}, and an intermediate frequency band at 790 cm^{-1}. In the high frequency band there is a peak at 1070 cm^{-1} and the other peak appears at 1200 cm^{-1}. With respect to experiment,[36,38,39] and the size of our model (192 atoms) the calculated VDOS shows good agreement as regards the location of the principal peaks and the distribution of their intensities.

D. SiSe$_2$ glass

In Fig. 12 we display the VDOS along with the principal peak positions in glassy SiSe$_2$. The general shape of the den-
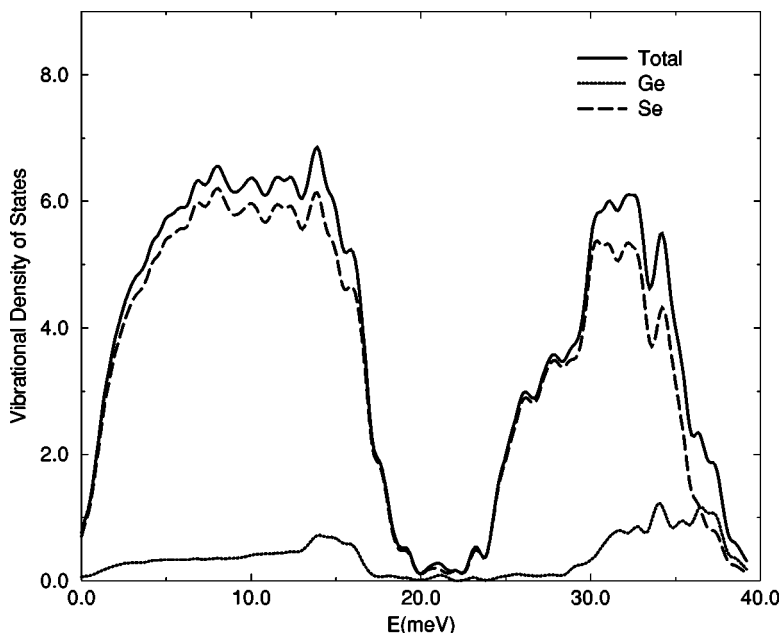
FIG. 10. Vibrational density of states (solid lines) and species projected vibrational density of states for Se (dashed lines) and Ge (dotted lines) for g-GeSe$_4$.

sity of states agrees well with the inelastic neutron scattering measurements made on the high-resolution medium-energy chopper spectrometer (HRMECS).[40] In the HRMECS experiment, the acoustic band reveals considerable structure, with three peaks, approximately centered at 48, 81, and 113 cm^{-1}. In our theoretical calculation, these peaks are, respectively, found at 47.5, 70, and 112 cm^{-1}; numbers quite consistent with inelastic neutron scattering experiment and Raman measurements.[28,34,41,42] In the intermediate band two peaks appear at 215 and 240 cm^{-1}. On Raman measurements the 48 cm^{-1} peak is unresolved. Based on Raman measurements, Susman et al.[28] associated the 70 cm^{-1} peak with the edge-sharing tetrahedra while Griffiths et al.[41] associated it to an A_g mode. More peaks are observed in the spectrum of the VDOS of g-SiSe$_2$. In our model these peaks occur around 215, 240, 303, 358, 387, and 469 cm^{-1}. Sugai[34] assigned the 213 and 222 cm^{-1} Raman peaks to the A_1 (corner sharing)

and the 240 and 248 cm^{-1} (not present in our model) to the ES modes. Jackson and Grossman[2] confirmed this result by assigning the 214 cm^{-1} peak to A_1 modes of CS-connected tetrahedra, either isolated or in chains.

V. ELECTRONIC PROPERTIES

The electronic properties of our models are analyzed through the electronic density of states (EDOS) and inverse participation ratio (IPR), which we denote by $\mathcal{I}$. The EDOS was obtained by summing suitably broadened Gaussians centered at each eigenvalue. The IPR

$$\mathcal{I}(E) = N \sum_{n=1}^{N} q(n,E)^2$$

determines the localization of electronic eigenvalues. Here N is the number of atoms in the model and $q(n,E)$ is the Mul-
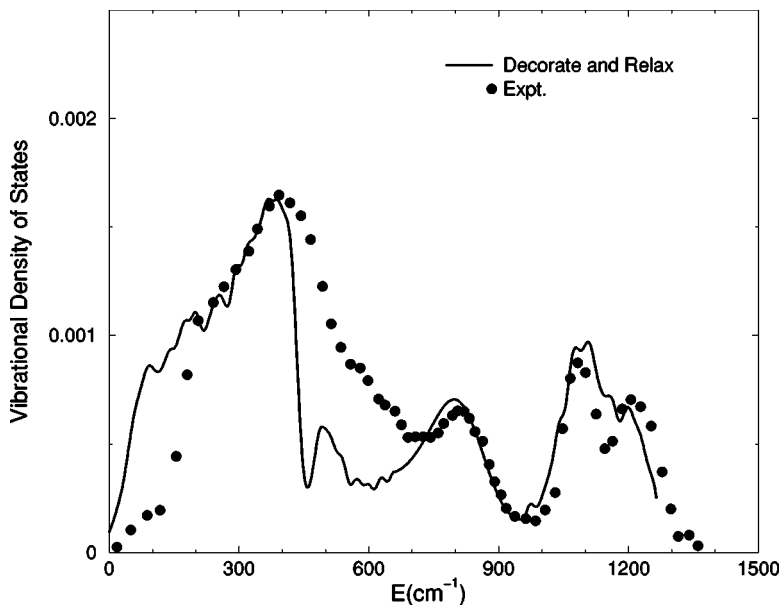

FIG. 11. Calculated vibrational density of states of 192 atom model of g-SiO$_2$ compared to neutron scattering experiments (Ref. 36).
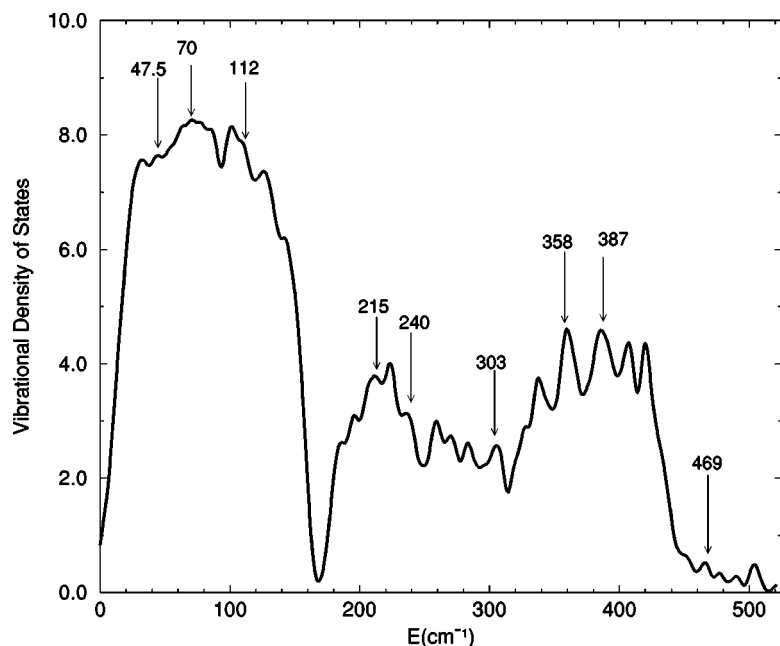
FIG. 12. Calculated vibrational density of states of g-SiSe$_2$. Principal peaks positions are shown.

liken charge localized on atomic site n in a certain eigenstate E. Hence, $\mathcal{I}$ is a measure of the inverse number of sites involved in the state with energy E. For a uniformly extended state, the Mulliken charge contribution per site is uniform and $\mathcal{I}(E) = 1/N$. For an ideally localized state, only one atomic site contributes all the charge and $\mathcal{I}(E) = 1$. Therefore a larger value of $\mathcal{I}$ means that the eigenstate is more localized in real space.

A. GeSe$_4$ glass

The EDOS is obtained by convoluting each energy eigenvalue with suitably broadened Gaussian. The calculated
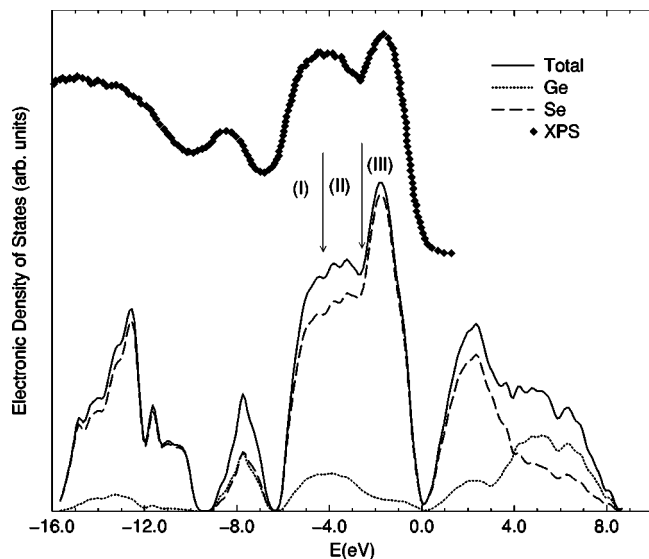

FIG. 13. Electronic density of states (solid lines) and species projected electronic density of states for Se (dashed lines) and Ge (dotted lines) for g-GeSe$_4$ obtained from *ab initio* simulations and compared to the XPS (Ref. 43) results. The Fermi level is at $E = 0$.

EDOS of g-GeSe$_4$ in Fig. 13 agrees quite well with experimental results obtained from x-ray photo-emission[43] (XPS). The substantial splitting between the first two peaks of the valence bands is also well-pronounced. The valence band exhibits three features. The two lowest bands between -15.64 and -6.5 eV originate from the atomic s-like states of Ge and Se. The next band contains p-like bonding states lying between -6.37 and -3.6 eV and predominantly p-like nonbonding states in the topmost valence region (our electronic eigenvalues have been shifted in order to place the valence band edge eigenvalue at zero).

The characteristic of the p band in g-GeSe$_4$ is represented by three distinct groups of peaks as indicated in the spectra of Fig. 13. The first group (I) contains all the bonding states whose energies fall within $[-6.0, -4.09]$ eV. The second group (II) includes the bonding states with energies in $[-4.09, -2.6]$ eV. The last group (III) is in the topmost region of $[-2.6, 0.0]$ eV. There is a substantial splitting between groups (II) and (III) giving rise to two peaks. These characteristics have been observed in g-GeSe2 (Ref. 44) and have been named the A_1 and A_2 peaks, respectively. By analogy to GeSe$_2$, the shoulder in group (I) has been identified as A_3 peak and the peak of the second lowest band as B peak. In Table VII we compare the positions of the peaks in the EDOS to the experimental results of GeSe$_2$.[44]

TABLE VII. The positions of the A_1, A_2, A_3 and B peaks in the EDOS of GeSe$_4$ and SiSe$_2$ glasses compared to experimental results of GeSe$_2$ (Ref. 44).

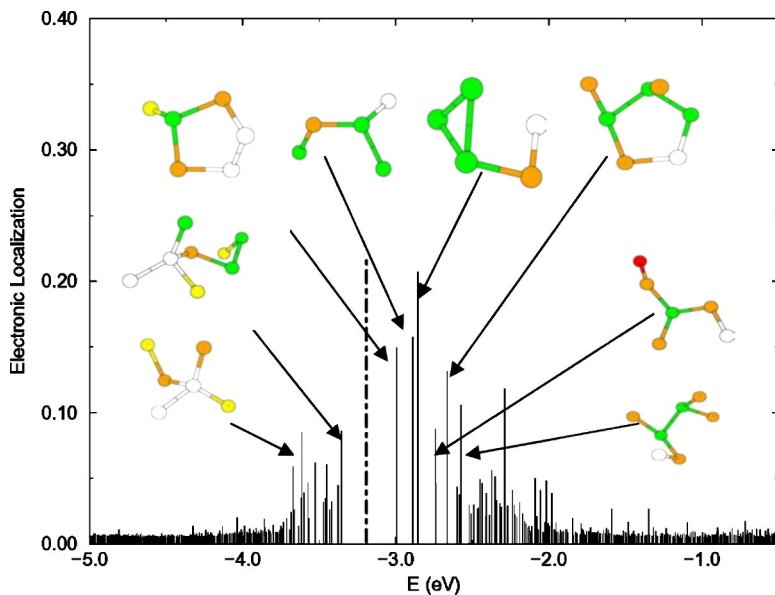| (eV)	A_1	A_2	A_3	B
Experiment GeSe$_2$	-1.38	-3.0	-4.6	-7.8
Quench from the melt GeSe$_4$	-1.7	-3.1	-4.6	-7.7
Quench from the melt GeSe$_9$	-1.36	-3.16	-4.62	-7.1
Decorate SiSe$_2$	-1.4	-2.86	-4.4	-7.3

FIG. 14. (Color online) Inverse participation ratio along with the characteristic defect types causing localization of electronic eigenstates in the band gap region of g-GeSe$_4$. The vertical dotted line indicates the position of the Fermi level. The color codes are defined as threefold Ge atoms (red), fourfold Ge atoms (white), threefold Se atoms (green), twofold Se atoms (orange), and onefold Se atoms (yellow).

In order to connect localized eigenstates to particular topological/chemical irregularities we plot in Fig. 14 the IPR in the band gap region along with the defect sites. It is valuable to know how the defect sites manifest themselves in the electronic eigenstates. A close look at the localized states at the band edges shows that the localized states at the top of the valence band are mostly associated with twofold and onefold Se atoms with at least one homopolar bond, whereas the localization at the conduction band edge arises from over-coordinated (threefold) Se atoms involved with at least one homopolar bond and from twofold-coordinated Se atoms involved with at least one wrong bond. A detailed examination shows that the localization of the eigenstates is mostly due to Se—Se bonds—connected with some defect sites. Figure 14 shows the typical defects structures causing the localization of eigenstates in the band gap region.

B. GeSe$_9$ glass

In Fig. 15 we plot the calculated EDOS and the species projected density of states of our model along with the XPS experimental results.[43] There is a good agreement between the experiment and the theory. All the relevant experimental features are found also in the calculated EDOS, providing further support for the validity and accuracy of our model. The g-GeSe$_9$ EDOS is very close to the Se EDOS.[45] The species projected density of states show that Se atoms contribute most to the spectrum. Hence, the lowest bands $[-15.0, -6.0]$ eV represent essentially the atomic s-like states of Se and Ge. The next band which lies between -6.0 and -2.2 eV contains p-like bonding states. Finally the topmost valence states are predominately nonbonding p-like in nature. Schlüter et $al.$[45] have shown that the lower energy peak in the p-like bonding states of Se represents states involved in intrachain bonding whereas states in the higher energy peak of the p-like bonding states arise in part from hybridization and contribute to the inter-chain bonding in the crystal. This argument holds for our model due to the large contribution of Se in the EDOS. The calculated Γ point optical

gap is of the order of 1.73 eV. It is rather interesting that there are no band-gap states in our EDOS. By analogy to g-GeSe$_2$, we can name the principal peaks as A_1, A_2, A_3, and B, respectively. Their values are listed on Table VII.

In Fig. 16 we plot $\mathcal{I}$ along with the defect types causing localization of electronic eigenstates in the band gap region. The states near the band edge are well localized. It is found that the highest occupied molecular orbital (HOMO) is localized on onefold coordinated Se connected to threefold Se, and on Se$_2$ bridge tetrahedra units. The localization at the conduction band edge is partly due to the over-coordinated Se atoms associated with at least one Se—Se homopolar bond, and one over-coordinated Ge atom connected to threefold Se atoms. In our g-GeSe$_9$ the electronic eigenstates are less localized compared to g-GeSe$_4$ and g-SiSe$_2$.
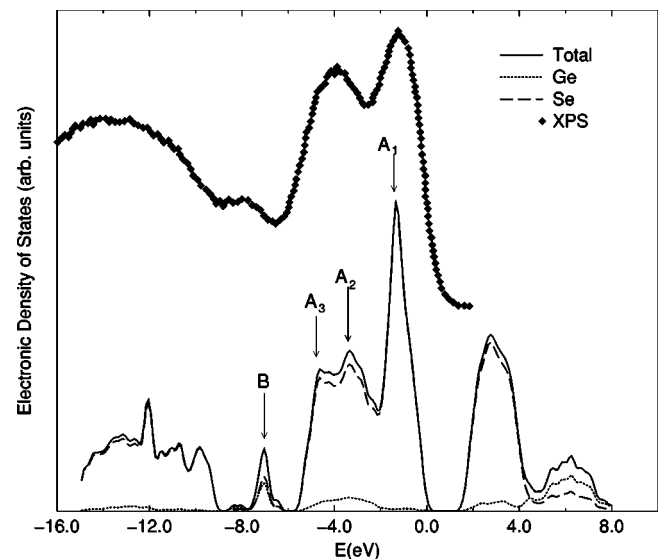

FIG. 15. Electronic density of states (solid lines) and species projected electronic density of states for Se (dashed lines) and Ge (dotted lines) for g-GeSe$_9$ obtained from ab $initio$ simulations and compared to the XPS (Ref. 43) results. The Fermi level is at $E=0$.
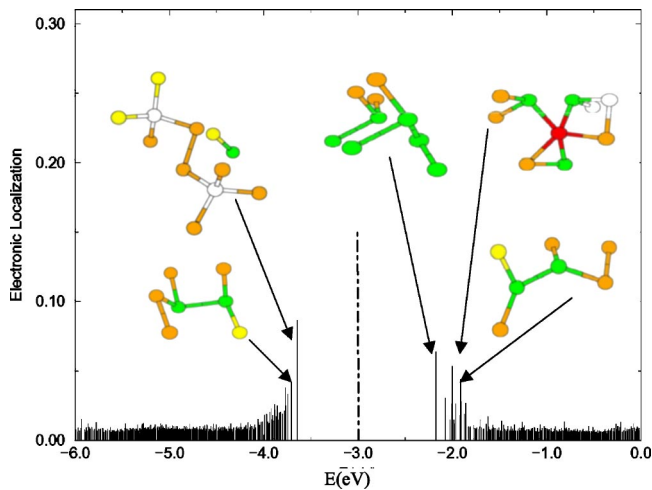
FIG. 16. (Color online) Inverse participation ratio along with the characteristic defect types causing localization of electronic eigenstates in the band gap region of g-GeSe$_9$. The vertical dotted line indicates the position of the Fermi level. The color codes are defined as threefold Ge atoms (grey), fourfold Ge atoms (white), fivefold Ge atoms (red), threefold Se atoms (green), twofold Se atoms (orange), and onefold Se atoms (yellow).

C. SiO$_2$ glass

Here we report the calculated EDOS for the 648-atom model of g-SiO$_2$. The EDOS (Fig. 17) is in very good agreement with the x-ray photoemission spectra (XPS)[46,47] and is comparable to the model of Sarnthein and co-workers.[48] Experimentally,[46,49,50] the electronic structures of crystalline and amorphous SiO$_2$ are known to be very similar. In the occupied states three regions can be distinguished; the low-energy region at -20 eV is associated with oxygen $2s$ states. The intermediate-energy region, -11 to -5 eV, which is strong bonding in character, involves bonding states between Si sp hybrids and O p orbitals; whereas the highest energy band composed of both weak-bonding and lone pair states (above -5 eV) arises from O p nonbonding orbitals.

D. SiSe$_2$ glass

The calculated EDOS and the species projected density of states are reported in Fig. 18. The valence band of the EDOS consists of two main bands. The upper band is from 0 to about -5 eV below the HOMO. For instance the Γ point optical gap of our model is of the order of 1.7 eV. As usual in local density approximation calculations, the experimental gap is substantially underestimated. To our knowledge, experimental information about the EDOS is unavailable for g-SiSe$_2$, so the curve in Fig. 18 is actually a *prediction*. The states can be classified in the following way: the states at about -14 eV are Se s states; the states from -8.3 to -3.3 eV are bonding states between Si sp^3 hybrids and Se p nonbonding orbitals. There is a distinctive peak deriving mainly from Se atoms. The leading peak is attributed to the lone-pair band of Se,[45] which is similar to topmost valence band of Se.[51] By analogy to GeSe$_2$, four peaks can be identified as A_1, A_2, A_3, and B peaks, respectively. Their values are listed on Table VII.

In Fig. 19 we plot the localization of electronic eigenstates for g-SiSe$_2$ in the band gap region. We also plot some of the characteristic defect types causing localization of electronic eigenstates in the band gap region. Eigenstates in the region $[-6,-5.3]$ eV of the valence band are quite extended, but as one approaches the valence band edge the eigenstates become increasingly localized. At the conduction band edge the states are also localized. As one moves away from the conduction band edge the states become less and less localized. By examining the localized states at the band edges we found that the localized states mostly derive from under-coordinated (threefold) Si atoms and over-coordinated three-fold Se atoms involved with Se—Se homopolar bonds. The localized states at the conduction band edge are mostly due to over-coordinated (threefold) Se atoms involved with ho-
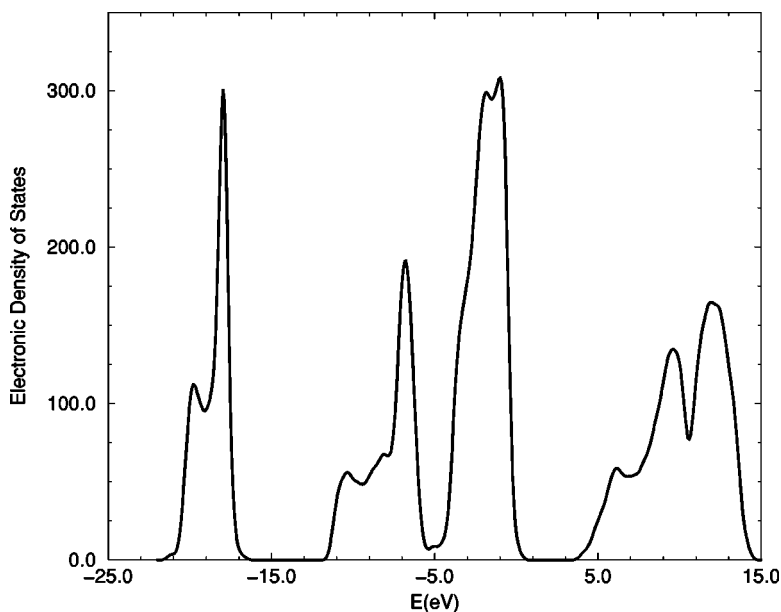

FIG. 17. Electronic density of states of g-SiO$_2$. The Fermi level is at $E=0$.
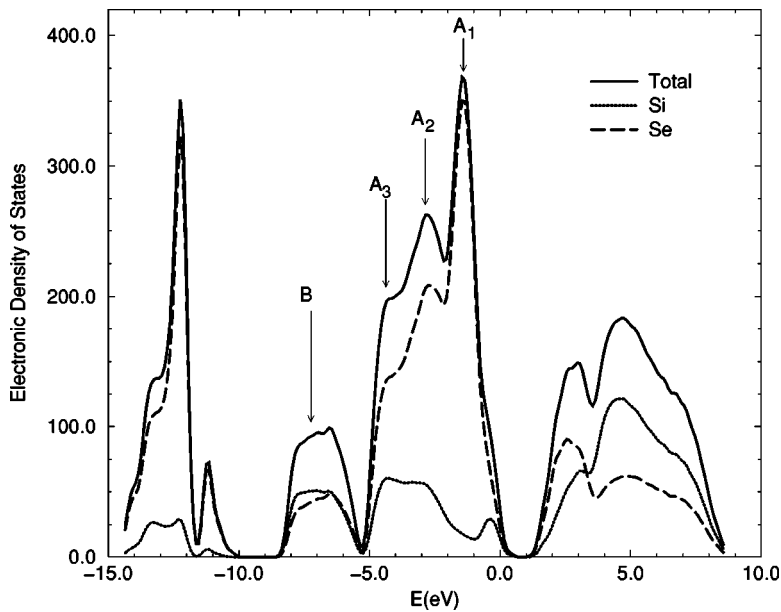
FIG. 18. Predicted electronic density of states (solid lines) and species projected electronic density of states for Se (dashed lines) and Si (dotted lines) for g-SiSe$_2$. The Fermi level is at $E=0$.

mopolar bond. The Se and Si IPRs reveal that the localization is more pronounced on Se atoms than on Si. We can conclude that Se—Se wrong bonds cause more localized states than the geometrical defectives structures.

VI. COMPOSITION-DEPENDENT TRENDS IN Ge$_x$Se$_{1-x}$ GLASSES

Having fully analyzed the structural, vibrational, and electronic properties of GeSe$_4$ and GeSe$_9$, we illustrate in this section the composition dependent trends in Ge$_x$Se$_{1-x}$ glasses. Other studies on the composition dependence of the glass structure have been made using both direct and indirect methods, extended x-ray absorption fine structure (EXAFS),[18] x-ray emission[52] and Raman spectroscopy.[34,53,54] In both experiment and our work, the medium-range order associated with Ge—Ge correlations, which is manifested by a FSDP varies as a function of x (Ge concentration). In GeSe$_9$, this peak appears only as a shoulder as opposed to

GeSe$_4$ where it is well pronounced. As x increases the intensity of the FSDP increases and reaches its maximum at $x=0.33$. Another relevant measure is the ratio of CS to ES tetrahedra as a function of x. The ratio of CS to ES tetrahedra increases with Ge concentration. In GeSe$_9$ ($x=0.1$) the structural motifs are Se-chain segments cross-linked by Ge(Se$_{1/2}$)$_4$ with negligible ratio of CS to ES tetrahedra. The addition of Ge imposes the disappearance of Se chains and the existence of Ge(Se$_{1/2}$)$_4$, and CS and ES tetrahedra.

The vibrational density of states of Ge$_x$Se$_{1-x}$ glasses is also composition-dependent. Since the (A_1-A_{1c}) band is associated to the breathing mode tetrahedra Ge(Se$_{1/2}$)$_4$, it should vary as a function of Ge concentration. In GeSe$_9$, the A_1 band appears as a shoulder due to the small concentration of tetrahedra. As x increases, the A_1 mode arises in the gap.

In the same way the electronic density of states is function of x. When x increases the intensity of the Ge band increases, but this band remains narrow. On the other hand, the width of the Se band remains constant, but its shape varies. The
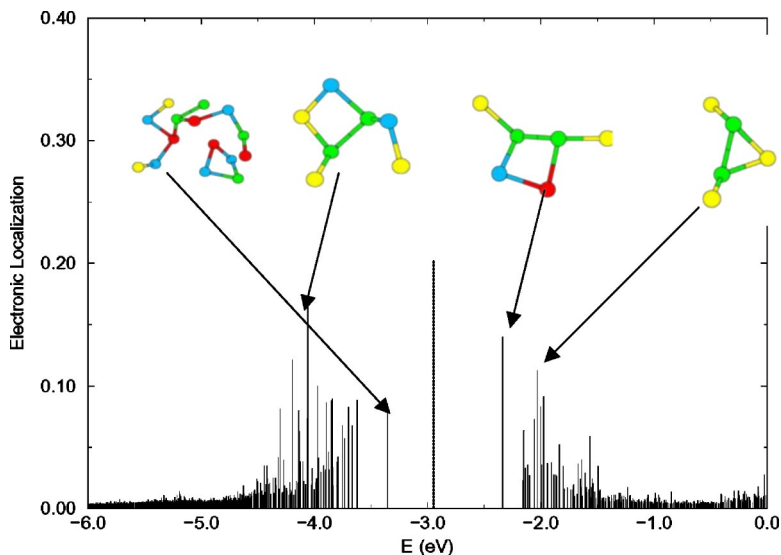

FIG. 19. (Color online) Inverse participation ratio along with the characteristic defect types causing localization of electronic eigenstates in the band gap region of g-SiSe$_2$. The vertical dotted lines indicates the position of the Fermi level. The color codes are defined as threefold Si atoms (red), fourfold Si atoms (yellow), threefold Se atoms (green), and twofold Se atoms (blue).

splitting between the A_1 and A_2 peaks becomes smaller, indicating the disappearance of Se chains.

This work supports the evidence of connectivity between the concentration of Ge, the atomic ordering associated with IRO, the (A_1-A_{1c}) band, and the shape of the Ge and Se bands in Ge_xSe_{1-x} glasses.

VII. DISCUSSION AND CONCLUSION

To illustrate the reliability and accuracy of our calculations, we give an example regarding $GeSe_2$. We made models of g-$GeSe_2$ using the decorate and relax method. The features of the models are reported elsewhere.[4,6] The topological ordering has been extensively studied using high level calculations. In the first approach the model obtained from FIREBALL has been fully relaxed with the plane wave code VASP (Ref. 55) to the nearest minimum. The second approach consists of annealing the original model using VASP. We observed that in both approaches the coordination number of Se atoms does not change significantly. A direct comparison with the one obtained from FIREBALL shows no meaningful difference. Li and Drabold[56] in their study of glassy AsSe have also found the same unexpected Se coordination. XPS experiments[57] on bulk glassy As_2Se_3 specimen prepared via the melt-quench method provide evidence for the existence of Se_3 and Se_1 as well in concentration up to $\sim 20\%$. In XPS experiments, Antoine *et al.*[57] observed that the two wrongly coordinated Se defects occur in about the same concentration. They found that 22.1%, 59.2%, and 18.7% of Se atoms are, respectively, onefold, twofold, and threefold coordinated. In a related vein, using density functional theory (DFT) to study the liquid $GeSe_2$, Massobrio *et al.*[58] found that as much as 25% of Se atoms were threefold coordinated and 2.2 were, respectively, onefold and fourfold coordinated. These results are somewhat surprising, and further modeling and experiment is needed to clarify the unexpected threefold and onefold Se coordination.

We have presented the results of a large scale computer simulation using a different approach from the usual quench from melt scheme for modeling some binary glasses. We have shown that for certain binary IV-VI glasses (especially silica), decoration of bond-centered column VI atoms on tetrahedral amorphous networks leads with appropriate rescaling and relaxation to highly realistic models of the IV-VI binary glasses. We investigated the topological structure, dynamics, and electronic structure of silica and silicon diselenide and compared with the experiments. Excellent agreement is found with the experimental data in the high Q

region for all the $S(Q)$ indicating that the short-range order is well reproduced for all configurations. In the low Q region, the appearance of the first sharp diffraction peak (peak amplitude and position) in $S(Q)$ and its partials describes the intermediate-range order. In the Bhatia-Thornton concentration-concentration structure factor of g-$SiSe_2$, a FSDP is observed, indicating concentration fluctuations over intermediate-range distances.

SiO_2 is strikingly good unlike $GeSe_2$, $SiSe_2$ which are good but not nearly so perfect. This may be due to the fact that silica consists entirely of corner sharing tetrahedra since our starting configuration already contains higher number of corner sharing, it makes easier to eliminate the few edge sharing present in the system. A simple decoration scheme works quite well for this system.

We also carried out first-principles molecular dynamics simulations to study the properties of $GeSe_4$ and $GeSe_9$. We performed a comparison between the results of our simulation and available experimental data. The comparison comprised the neutron structure factor and the vibrational density of states. The agreement with experiment is very good. We presented a detailed analysis of the atomic structure of these glasses. We found that the Ge-centered tetrahedra are the predominant coordination motifs in g-$GeSe_4$. In g-$GeSe_9$, the structure consists of Se-chain segments which are cross-linked by $Ge(Se_{1/2})_4$ tetrahedra. We investigated the intermediate-range order by calculating the partial and the Bathia-Thornton structure factors. We observed a FSDP in each partial and Bhatia-Thornton structure factors of $GeSe_4$. Finally we investigated the electronic properties of these glasses by computing the electronic density of sates and the inverse participation ratio. The IPR shows that the localization in the $SiSe_2$ and $GeSe_4$ glass is mostly due to homopolar bonds than the geometrical defectives structures.

[1] *The Physics and Technology of Amorphous SiO2*, edited by R. A. B. Devine (Plenum, New York, 1988).

[2] K. Jackson and S. Grossman, Phys. Rev. B **65**, 012206 (2001).

[3] S. Nakhmanson, Ph.D. thesis, Ohio University, 2001; http://www.phy.ohiou.edu/~drabold/serge; X. Zhang and D. A. Drabold, Phys. Rev. Lett. **83**, 5042 (1999).

[4] D. N. Tafen and D. A. Drabold, Phys. Rev. B **68**, 165208 (2003).

[5] P. Biswas, D. Tafen, and D. A. Drabold, Phys. Rev. B **71**, 054204 (2005); P. Biswas, D. N. Tafen, R. Atta-Fynn, and D. A. Drabold, J. Phys.: Condens. Matter **16**, S5173 (2004).

[6] D. A. Drabold, J. Li, and D. N. Tafen, J. Phys.: Condens. Matter **15**, 1529 (2003).

[7] M. Mitkova and M. N. Kozicki, J. Non-Cryst. Solids **299**, 1023 (2002).

[8] N. R. Rao, P. S. R. Krishna, S. Basu, B. A. Dasannacharya, K. S. Sangunni, and E. S. R. Gopal, J. Non-Cryst. Solids **240**, 221 (1998); N. R. Rao, K. S. Sangunni, E. S. R. Gopal, P. S. R. Krishna, R. Chakravarthy, and B. A. Dasannacharya, Physica B **213 & 214**, 561 (1995).

[9] A. A. Demkov, J. Ortega, O. F. Sankey, and M. Grumbach, Phys. Rev. B **52**, 1618 (1995).

[10] O. F. Sankey and D. J. Niklewski, Phys. Rev. B **40**, 3979 (1989); O. F. Sankey, D. A. Drabold, and G. B. Adams, Bull. Am. Phys. Soc. **36**, 924 (1991).

[11] For example, J. M. Soler, E. Artacho, J. D. Gale, J. Junquera, P. Ordejón, and D. Sanchez-Portal, J. Phys.: Condens. Matter **14**, 2745 (2002), and references therein.

[12] F. Wooten and D. Weaire, *Solid State Physics*, edited by H. Ehrenreich, D. Turnbull, and F. Seitz (Academic, New York, 1987), p. 40.

[13] G. T. Barkema and N. Mousseau, Phys. Rev. B **62**, 4985 (1996).

[14] I. Petri and P. S. Salmon, Phys. Chem. Glasses **43C**, 185 (2002).

[15] P. Vashishta, R. K. Kalia, J. P. Rino, and I. Ebbsjö, Phys. Rev. B **41**, 12 197 (1990).

[16] C. Massobrio, A. Pasquarello, and R. Car, Phys. Rev. Lett. **80**, 2342 (1998); Comput. Mater. Sci. **17**, 115 (2000).

[17] S. Susman, K. J. Volin, D. G. Montague, and D. L. Price, J. Non-Cryst. Solids **125**, 168 (1990).

[18] W. Zhou, M. Pasesler, and D. E. Sayers, Phys. Rev. B **43**, 2315 (1991).

[19] G. Lucovsky and T. M. Hayes, *Amorphous Semiconductors*, edited by M. H. Brodsky (Springer, Berlin, 1979), p. 125.

[20] XMOL, version 1.3.1, 1993, Minnesota Supercomputer Center, Inc., Minneapolis, MN 55415.

[21] P. A. V. Johnson, A. C. Wright, and R. N. Sinclair, J. Non-Cryst. Solids **58**, 109 (1983).

[22] R. F. Pettifer, R. Dupree, I. Farnan, and U. Sternberg, J. Non-Cryst. Solids **106**, 408 (1988).

[23] R. L. Mozzi and B. E. Warren, J. Appl. Crystallogr. **2**, 164 (1969).

[24] P. G. Coombs, J. F. De Natale, P. J. Hood, E. K. McElfresh, R. S. Wortman, and J. F. Schackelford, Philos. Mag. A **51**, L39 (1985).

[25] K. Vollmayr, W. Kob, and K. Binder, Phys. Rev. B **54**, 15 808 (1996).

[26] R. W. Johnson, D. L. Price, S. Susman, M. Arai, T. I. Morrison, and G. K. Shenoy, J. Non-Cryst. Solids **83**, 251 (1986).

[27] M. Celino, Ph.D. dissertation, Université Louis Pasteur, Strasbourg, 2002.

[28] S. Susman, R. W. Johnson, D. L. Price, and K. J. Volin, Mater. Res. Soc. Symp. Proc. **61**, 91 (1986).

[29] M. Celino and C. Massobrio, Phys. Rev. Lett. **90**, 125502 (2003).

[30] G. A. Antonio, R. K. Kalia, A. Nakano, and P. Vashishta, Phys. Rev. B **45**, 7455 (1992).

[31] M. Cobb, D. A. Drabold, and R. L. Cappelletti, Phys. Rev. B **54**, 12 162 (1996).

[32] B. Effey and R. L. Cappelletti, Phys. Rev. B **59**, 4119 (1999).

[33] W. A. Kamitakahara, R. L. Cappelletti, P. Boolchand, B. Halfpap, F. Gompf, D. A. Neumann, and H. Mutka, Phys. Rev. B **44**, 94 (1991).

[34] S. Sugai, Phys. Rev. B **35**, 1345 (1987).

[35] P. M. Bridenbaugh, G. P. Espinosa, J. E. Griffiths, J. C. Phillips, and J. P. Remeika, Phys. Rev. B **20**, 4140 (1979).

[36] M. J. Carpenter and D. L. Price, Phys. Rev. Lett. **54**, 441 (1985).

[37] C. T. Kirk, Phys. Rev. B **38**, 1255 (1988).

[38] F. L. Galeener and G. Lucovsky, Phys. Rev. Lett. **37**, 1474 (1976).

[39] A. Kucirková and K. Navrátil, Appl. Spectrosc. **48**, 113 (1994).

[40] M. Arai, D. L. Price, S. Susman, K. J. Volin, and U. Walter, Phys. Rev. B **37**, 4240 (1988).

[41] J. E. Griffiths, M. Malyj, G. P. Espinosa, and J. P. Remeika, Phys. Rev. B **30**, 6978 (1984); M. Malyj, G. P. Espinosa, and J. E. Griffiths, *ibid.* **31**, 3672 (1985).

[42] M. Tenhover, M. A. Hazle, and R. K. Grasselli, Phys. Rev. Lett. **51**, 404 (1983); M. Tenhover, M. A. Hazle, R. K. Grasselli, and C. W. Tompson, Phys. Rev. B **28**, 4608 (1983); M. Tenhover, R. S. Henderson, D. Lukco, M. A. Hazle, and R. K. Grasselli, Solid State Commun. **51**, 455 (1984).

[43] E. Bergignat, G. Hollinger, H. Chermette, and P. Pertosa, Phys. Rev. B **37**, 4506 (1988).

[44] S. Hino, T. Takaharshi, and Y. Harada, Solid State Commun. **35**, 379 (1980).

[45] M. Schlüter, J. D. Joannopoulos, and M. L. Cohen, Phys. Rev. Lett. **33**, 89 (1974); N. J. Shevchik, J. Tejeda, M. Cardona, and D. W. Langer, Solid State Commun. **12**, 1285 (1973).

[46] B. Fischer, R. A. Pollak, T. H. DiStefano, and W. D. Grobman, Phys. Rev. B **15**, 3193 (1977).

[47] R. B. Laughlin, J. D. Joannopoulos, and D. J. Chadi, Phys. Rev. B **20**, 5228 (1979).

[48] J. Sarnthein, A. Pasquarello, and R. Car, Phys. Rev. Lett. **74**, 4682 (1995).

[49] H. R. Phillip, Solid State Commun. **4**, 73 (1966); J. Phys. Chem. Solids **32**, 1935 (1971).

[50] E. Loh, Solid State Commun. **2**, 269 (1964); G. Klein and H. U. Chun, Phys. Status Solidi B **49**, 167 (1972).

[51] K. S. Liang, J. Non-Cryst. Solids **18**, 197 (1975).

[52] S. B. Mamedov, N. D. Aksenov, L. L. Makarov, and Y. F. Batrakov, J. Non-Cryst. Solids **195**, 272 (1996).

[53] X. Feng, W. J. Bresser, and P. Boolchand, Phys. Rev. Lett. **78**, 4422 (1997).

[54] Y. Wang, O. Matsuda, K. Inoue, O. Yamamuro, T. Matsuo, and K. Murase, J. Non-Cryst. Solids **232–234**, 702 (1998).

[55] G. Kresse and J. Furthmüller, Phys. Rev. B **54**, 11 169 (1996); Comput. Mater. Sci. **6**, 15 (1996); see also http://cms.mpi.univie.ac.at/vasp.

[56] J. Li and D. A. Drabold, Phys. Rev. B **61**, 11 998 (2000); **64**, 104206 (2001).

[57] K. Antoine, J. Li, D. A. Drabold, H. Jain, M. Viček, and A. C. Miller, J. Non-Cryst. Solids **326**, 248 (2003).

[58] C. Massobrio, A. Pasquarello, and R. Car, Phys. Rev. B **64**, 144205 (2001).